Representative Elementary Volume (REV) in Spatio-Temporal Domain: A Method to find REV for Dynamic Pores

Harpreet Singh[1, 2] (harpreet.singh@utexas.edu)
[1]The University of Texas at Austin, Austin, TX, USA
[2]Current Address: National Energy Technology Laboratory, Morgantown, WV, USA

ABSTRACT

One of the potential risks associated with subsurface storage of CO_2 is the seepage of CO_2 through existing faults and fractures. There have been a number of studies devoted to this topic. Some of these studies show that geochemistry, especially mineralization, plays an important role in rendering the faults as conduits for CO_2 movement while others show that mineralization due to CO_2 injection can result in seep migration and flow diversion. Therefore, understanding the changes in reservoir properties due to pore alterations is important to ensure safe long term CO_2 storage in the subsurface.

We study the changes in the *Representative Elementary Volume* (REV) of a rock due to reactive kinetics over a time, using a statistical approach and pore-scale CO_2-rock interaction data. The goal of this study is to obtain the REV of a rock property that accounts for pore-scale changes over time due to reactive kinetics, and we call this as spatiotemporal REV.

Scale-up results suggest that the REV changes with time when CO_2-rock interaction is considered. It is hypothesized that the alteration in pore structure introduces more heterogeneity in the rock, and because of this the magnitude of REV increases. It is possible that these noticeable changes in REV at pore-scale may have an impact when analyzed at the reservoir scale.

1 INTRODUCTION

CO_2 injection in a subsurface saline aquifer results in the formation of an acidic aqueous mixture that reacts with rock minerals and leads to dissolution and/or precipitation. This reaction between the acidic mixture of CO_2/brine and rock minerals eventually alters the underlying pore structure by changing the porosity, and, hence, the permeability (Gunter et al., 1997; Izgec et al., 2005, 2007; Johnson et al., 2004; Kim, 2012; Shipton et al., 2004). According to Pham et al., (2012; 2011), this modification of reservoir properties such as porosity and permeability is strongly system dependent. For example, CO_2-rock interaction of siliciclastic rocks is usually insignificant over thousands of years due to the balance between dissolution and precipitation and the minor binding of carbon in the rocks. The dissolution-precipitation reactions are even less pronounced in closed-system carbonate rocks, however, basalts may bind larger amounts of carbon and changes in porosity are more susceptible to CO_2-rock interaction. Recent

laboratory experiments by Miri et al., (2015) suggest that there can be massive precipitation of salt inside the CO_2 pathways due to surface energy effects and hydrophilic nature of salt. However, most of these studies, which are limited to monitoring the short-term effects of 2 to 4 weeks, lack any rigorous and systematic long-term CO_2 exposure to properly infer the combined geochemical and permeability effects on reservoir flow dynamics. A recent study by Rathnaweera et al., (2016) investigated 1.5 years of CO_2 exposure on combined geochemical and permeability effects on a sandstone sample under typical reservoir injection pressures (~5 MPa) and confining pressures (~20 MPa). According to Rathnaweera et al., (2016), this time frame is within the duration required to establish an equilibrium between the reactants and the resulting buffer solution formed when CO_2 initially dissolves in brine under reservoir conditions. After 1.5 years, they observed a drastic pH drop (49%), significant NaCl crystallization (salt) in the rock pore space by alteration, and substantial enhancement in permeability (~10-17%) due to the dissolution of pore-filling calcite and calcite coatings of detrital minerals. Even though the time required for mineral dissolution (such as initiation of the quartz reaction with CO_2 and brine) is considerably large on the order of geological time scale, according to Knauss and Wolery, (1988) and Davis et al., (2011), some rock minerals, such as carbonate (e.g. calcite, magnesite, siderite), can react with CO_2 and brine within a very short period of 2 to 4 weeks. Therefore, based on the work of Rathnaweera et al., (2016), it is safe to assume that CO_2 injection can cause significant pore alterations and potentially enhance the rock permeability. As per Rochelle et al., (2004), even this small alteration in rock permeability may impact the effectiveness of the field-scale CO_2 storage process. This has been verified at a field-scale CO_2 sequestration site by Arsyad et al., (2013), who noticed that CO_2 injection caused permeability enhancement in the Ainoura and Berea sandstone formations, rendering easy migration of CO_2 plumes into the upper cap-rock layers and posing a high risk of leakage into the surrounding groundwater aquifers. According to Le Borgne and Gouze, (2008), these changes in the subsurface parameters is a function of the temporal correlations controlled by small-scale structures in addition to the spatial correlations of the geological features.

Therefore, a scale-up procedure that accounts for uncertainty in the magnitude of reservoir property introduced due to reactive dynamics over time is required. Broadly speaking, the objective of scale-up is to find the spatial variability of an attribute at a coarser scale given the variability at a finer scale (Singh and Srinivasan, 2014b). This concept underlies the notion of the *Representative Elementary Volume* (REV), which is the volume at which the averaging of the reservoir attribute becomes stable (Bear, 1972). This study aims to obtain the REV of a rock property by accounting for spatial and temporal variations in that property due to reactive kinetics. The REV for conservative process is modeled using the 3-D pressure data and the REV for reactive process is modeled using three different types of data – fluid/matrix pore geometry alteration data, porosity change (due to dissolution) data, and volume-based dimensionless CO_2 concentration data – all in 2-D spatial snapshots at various time instants. Scaling characteristics of attributes pertinent to both conservative process and reactive process

are presented and compared with discussions. Finally, the importance of this research work is highlighted. To illustrate the application of this method on tangible parameters, we find the spatiotemporal REV for a reaction rate constant for simple first-order reaction kinetics.

2 METHOD AND ANALYSIS

2.1 Statistical Scale-up Method

The variance of mean of any attribute f at some volume support (or scale) depicts the variability of the volume average (spatial average or spatio-temporal average) at that particular volume scale. This variance of mean is likely to be large at short scales and it should decrease with the increase in scale. The REV of an attribute can be determined from a log-log plot of the variance of attribute's *linear average* as a function of length scale (Lake and Srinivasan, 2004). This variance of mean plot depicts the diagnostic signature of a negative unit slope at scales larger than REV as illustrated in Figure 1. The slope value signifies independence between the block means at that scale.

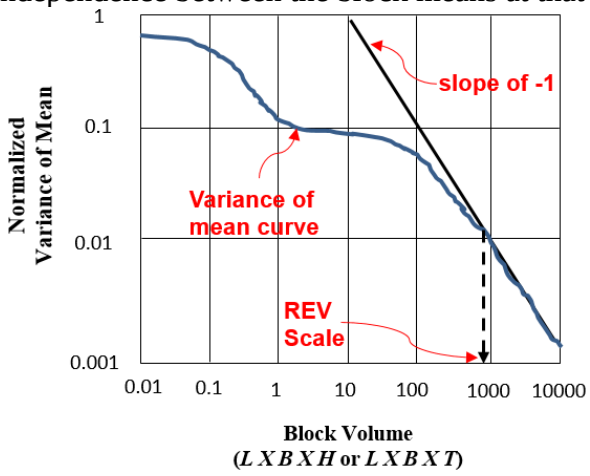

Figure 1: REV scale from statistical method that requires "variance of mean" values corresponding to different block volumes. REV scale is obtained when "variance of mean" curve approaches -1 slope

2.1.1. Variance of mean

The variance of the mean of any attribute f can be computed on a 3-D space or on a 3-D space-time domain by integrating the space or space-time correlation function, respectively, of attribute f as shown by Eqn. (1) and Eqn. (2), respectively:

$$Var(\overline{f}) = \frac{2\sigma^2}{(V)^2}\left(\int_{\zeta_3=0}^{\zeta_3=H} \int_{\eta_3}^{\eta_3=\zeta_3} \int_{\zeta_2=0}^{\zeta_2=B} \int_{\eta_2}^{\eta_2=\zeta_2} \int_{\zeta_1=0}^{\zeta_1=L} \int_{\eta_1}^{\eta_1=\zeta_1} \rho_{corr}\left\{\eta_1(L), \eta_2(B), \eta_3(H)\right\} d\eta d\xi \right) \quad (1)$$

$$Var(\overline{f}) = \frac{2\sigma^2}{(V)^2}\left(\int_{\zeta_3=0}^{\zeta_3=T} \int_{\eta_3}^{\eta_3=\zeta_3} \int_{\zeta_2=0}^{\zeta_2=B} \int_{\eta_2}^{\eta_2=\zeta_2} \int_{\zeta_1=0}^{\zeta_1=L} \int_{\eta_1}^{\eta_1=\zeta_1} \rho_{corr}\left\{\eta_1(L), \eta_2(B), \eta_3(T)\right\} d\eta d\xi \right) \quad (2)$$

where,

σ^2 = variance of attribute f

ρ_{corr} = spatial autocorrelation function

η = all possible lags within the spatiotemporal region

V = Volume over which scale-up is investigated

(for 3D spatial volume and spatiotemporal volume, V is $L \times B \times H$ and

$L \times B \times T$, respectively)

L, B, H, T = length, breadth, height, and total time, respectively

In order to find REV as illustrated in Figure 1, we need "variance of mean" values corresponding to different block volumes. The "variance of mean" values can be calculated from two different approaches depending on what type of data is available. These two approaches are depicted by the left hand side (LHS) and right hand size (RHS), respectively, of above two equations. That is, variance of mean can be calculated either numerically over various spatial (or spatial-temporal) scales as depicted by LHS of above equations, or analytically using correlation function as depicted by RHS of above equations. The correlation function can either be a covariance or variogram model (Deutsch and Journel, 1997) of the parameter for which REV is to be calculated.

2.1.2. Workflow to find REV

Using fine-scale values:

If fine-scale values of the parameter for which REV is to be calculated are available, then the "variance of mean" can be computed as shown pictorially in Figure 2. This figure illustrates the workflow needed to find the curve presented in Figure 1 from which REV is obtained. As shown in Figure 2, there are four steps needed in order to estimate the curve shown in Figure 1, which are: i) for a given size of block volume, find the variance of each block volume from the coarse model, ii) take the mean of variances calculated in step #i, iii) repeat previous two steps for different sizes of block volume, and iv) use the "variance of mean" values calculated for different sizes of block volume to obtain REV as illustrated by Figure 1.

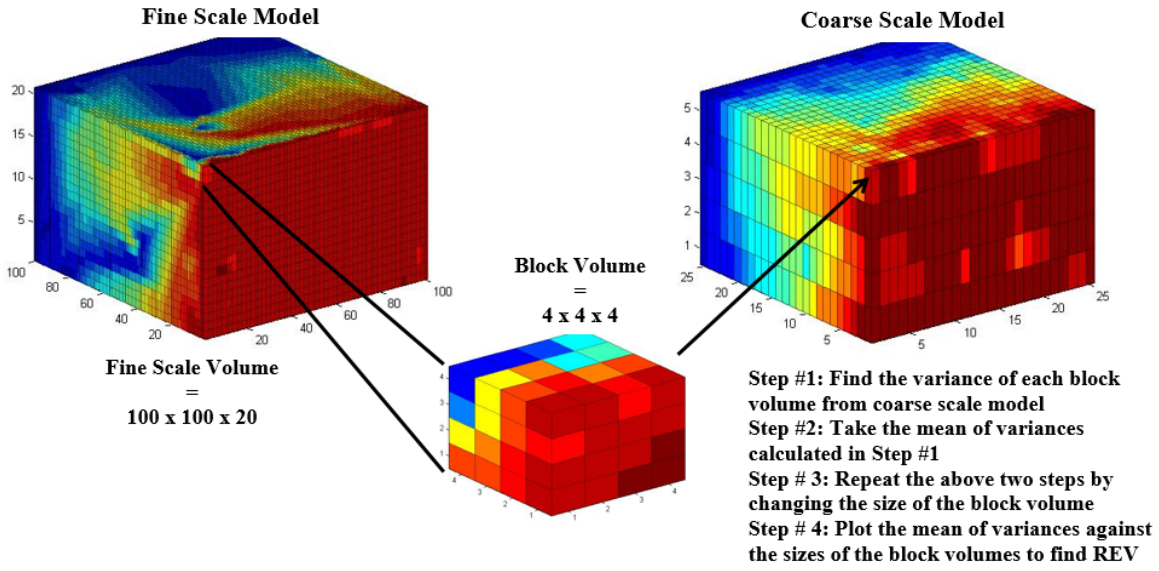

Figure 2: Workflow to find "variance of mean" values that are used to obtain REV scale as shown in Figure 1

Using correlation function of the parameter:

The general procedure to estimate variance of mean plot using the correlation function (for e.g. variogram model) is by numerically integrating the variogram at the point support volume for all possible lag distances (block volume is the product of those lag distances) over the volume of investigation. This will give variance of mean value for each block volume, and repeating this over increasing sizes of lags would give the curve shown in Figure 1 from which REV is obtained. For further discussions on space-time correlations and the how to estimate variogram values, readers can refer elsewhere (e.g. Singh, 2014; Singh and Srinivasan, 2014b).

Theoretically, the variance of the mean plot computed using either the fine-scale numerical values of the parameter or its variogram should be similar; however, there is usually some difference in the two results because of error in performing the numerical integration and also in approximating the empirical variograms using simplified positive definite variogram models. The example given in later section illustrates this fact.

To our knowledge, most of the existing scale-up methods consider only spatial scale-up at a particular instant in time (Lake and Srinivasan, 2004; Leung and Srinivasan, 2011). Specifically, other scale-up methods such as the volume averaging and other random walk models based on partial differential equations (PDE) assume pseudo steady state condition and a homogeneous or a periodic medium. Leung and Srinivasan, (2011), and Vishal and Leung, (2015) have used volume averaging to scale-up effective mass transfer coefficient, but it is limited for a particular snapshot of time assuming pseudo steady state condition. However, some processes that alter reservoir properties require investigation of scale-up jointly in space and time. Even though it is possible to describe

the combined spatial and temporal scaling of reactive processes using random walk approach (Sund et al., 2015), it is limited to only homogeneous or periodically varying media. The method proposed above does not require assumption of either pseudo steady state condition or a periodic medium, and hence, it can be used to scale-up a naturally heterogeneous medium in a combined space-time domain.

2.2 Pore-Scale Data

The data used in the statistical scale-up analysis is obtained from the work of Ovaysi and Piri, (2010, 2014), where the authors simulate pore-scale reactive flow due to CO_2 injection inside a sample which is assumed to be completely composed of calcium carbonate. Below, we briefly describe the characteristic of the porous media used in their simulations and the scheme used by Ovaysi and Piri, (2010, 2014) to simulate the reactive CO_2 flow inside a rock. For detailed discussions on the mathematical modeling and the parameters used for the pore-scale simulation results readers may refer to the work by Ovaysi and Piri, (2010, 2014).

2.2.1 Porous Media Characteristics

Ovaysi and Piri, (2010, 2014) used the high resolution images of a rock sample (at 3.398 μm) assumed to be completely composed of calcium carbonate acquired using computed microtomography by Dong, (2007) to simulate the fluid flow inside the sample at the pore-scale. Even though this assumption is not consistent with the mineralogy of Berea sandstone, Ovaysi and Piri, (2014) base this assumption on a vastly different pore space topologies (Blumenfeld et al., 2013; Øren and Bakke, 2003) for pore-size distributions. It is the impact of different pore-space topologies on dissolution/precipitation patterns that was investigated in their work, and hence, the original mineralogy of the rock was not the main focus of their study. The porosity and permeability of this sample was 22.7% and 980 mD, respectively. Furthermore, to simplify the computational expense and to shorten the time required to see changes in porosity and permeability, smaller samples were selected to significantly reduce the time of the simulations.

2.2.2 Chemical Reactions and Kinetics

For the porous media considered, only the chemical reactions occurring between the calcite and brine are considered. Seven reactions are considered and listed in Table I; in particular, four reactions are homogeneous where equilibrium is achieved instantly, whereas the other three reactions are heterogeneous surface reactions that proceed slowly as per their respective rate constants. The equilibrium reactions in used in Ovaysi and Piri, (2014) are treated as per the method described by Lichtner et al., (1996), whereas the equilibrium constants and the reaction rates are taken from Ellis et al., (2010) and Chou et al., (1989), respectively. The reactive surface area is calculated by estimating the amount of mass gained/lost for surface solids by growing/shrinking as a result of the

kinetic reactions. This mass is used to find the extent of shrinkage/growth that is used in an analytical expression for the reactive surface area. Since the mass of shrinkage/growth continuously changes with time, therefore, the estimated reactive surface area also changes with time. The sample was first saturated with water at a 1.2 M ionic strength and pH = 7 at 25 ^{o}C. Then a highly acidic brine solution with pH = 1 is injected into the sample made entirely of calcium carbonate. The reactive model used in Ovaysi and Piri, (2014) was validated against the microfluidic reactive flow experiment performed by Li et al., (2008).

Table I: Chemical reactions

Reactions	Type of Reaction
$H_2O \Leftrightarrow H^+ + OH^-$	Equilibrium
$CO_2 + H_2O \Leftrightarrow H_2CO_3$	Equilibrium
$H_2CO_3 \Leftrightarrow HCO_3^- + H^+$	Equilibrium
$HCO_3^- \Leftrightarrow CO_3^{2-} + H^+$	Equilibrium
$CaCO_3 + H^+ \Rightarrow Ca^{2+} + HCO_3^-$	Heterogeneous (surface)
$CaCO_3 + H_2CO_3 \Rightarrow Ca^{2+} + 2HCO_3^-$	Heterogeneous (surface)
$CaCO_3 \Leftrightarrow Ca^{2+} + CO_3^{2-}$	Heterogeneous (surface)

2.2.3 Flow and Transport Simulation Scheme

The pore-scale data used in this work is taken from the work of Ovaysi and Piri, (2014) who used a modified moving particle semi-implicit (MMPS) technique originally proposed by Ovaysi and Piri, (2010) to model the flow of incompressible and compressible fluids inside the pore space characterized from high-resolution images of a sandstone sample. The MMPS method is a Lagrangian particle based approach that has been validated against analytical and numerical models, and with experimental data available in the literature. For more information on the MMPS method and the values of various parameters used in the original simulation studies, readers may refer to the pore-scale modeling work by Ovaysi and Piri, (2010, 2011, 2013, 2014).

Pore-scale data is simulated in 3-D for conservative processes and reactive processes, respectively. Simulated data for the reactive processes is obtained for t = 0 to t = 20 sec in intervals of 2 sec and it is assumed the system reaches close to equilibrium. This is assumed to simplify the computational expense and to shorten the time required to see changes in porosity and permeability.

2.2.4 Resultant Data

The pore-scale simulation data for conservative and reactive processes is available in the form of point estimate (scattered) values. The Delaunay triangulation technique, as implemented in the Matlab® function directory ("TriScatteredInterp," R2013b) is

employed to interpolate the scattered data over a 3-D grid. Gridded data renders the task of variogram inference and modeling easier.

2.2.4.1 Data without Reactions (Advection-Diffusion Process)

The scattered pressure data and its interpolation in 3-D space for a conservative process is shown in Figure 3 (a) and (b), respectively.

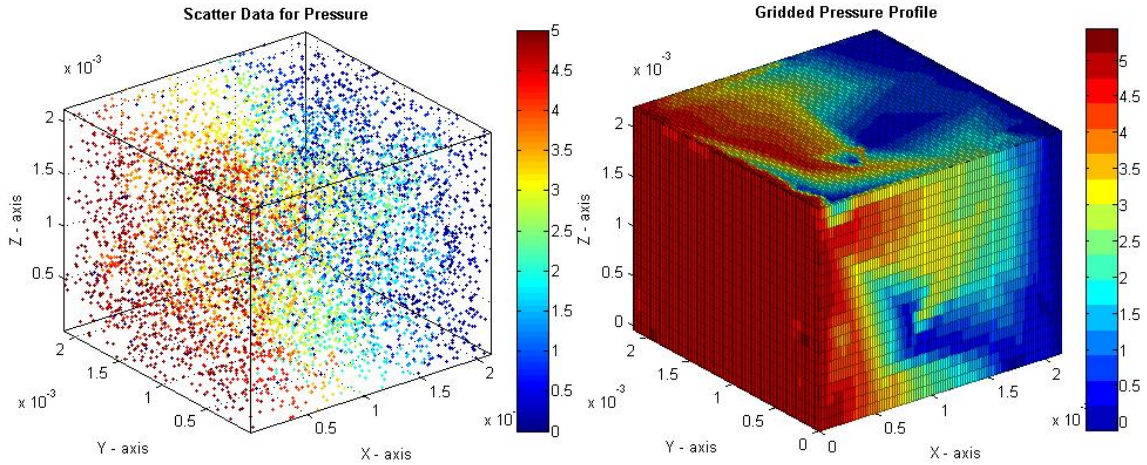

(a) (b)

Figure 3: Pressure data (in Pa) in 3-D space: (a) original scattered data points; (b) interpolated gridded dataset

2.2.4.2 Data with Reactions (Advection-Diffusion-Reaction Process)

Scattered data of three attributes at t = 20 sec, which are: 1) pore geometry alteration (PGA) data (legend = 0, 1 for matrix and fluid, respectively), 2) change in porosity (CIP) due to dissolution, i.e. $1 - \left(\frac{\Delta\phi}{\phi}\right)$, and 3) volume-based dimensionless CO_2 concentration (CO2CONC), is shown in Figure 4 (a). Since attribute PGA is merely a binary representation of fluid or matrix, it does not have any physical unit. CIP depicts the change in porosity in fractions; therefore, it is also dimensionless; for example, CIP = 1 denotes no change in matrix mass compared to its initial mass, and CIP = 0 denotes that there is no remaining mass of matrix due to complete dissolution. The corresponding gridded data of PGA, CIP and CO2CONC interpolated via the Delaunay triangulation technique is shown in Figure 4 (b). The number of grid blocks along X, Y and Z directions are 100, 100 and 20, respectively.

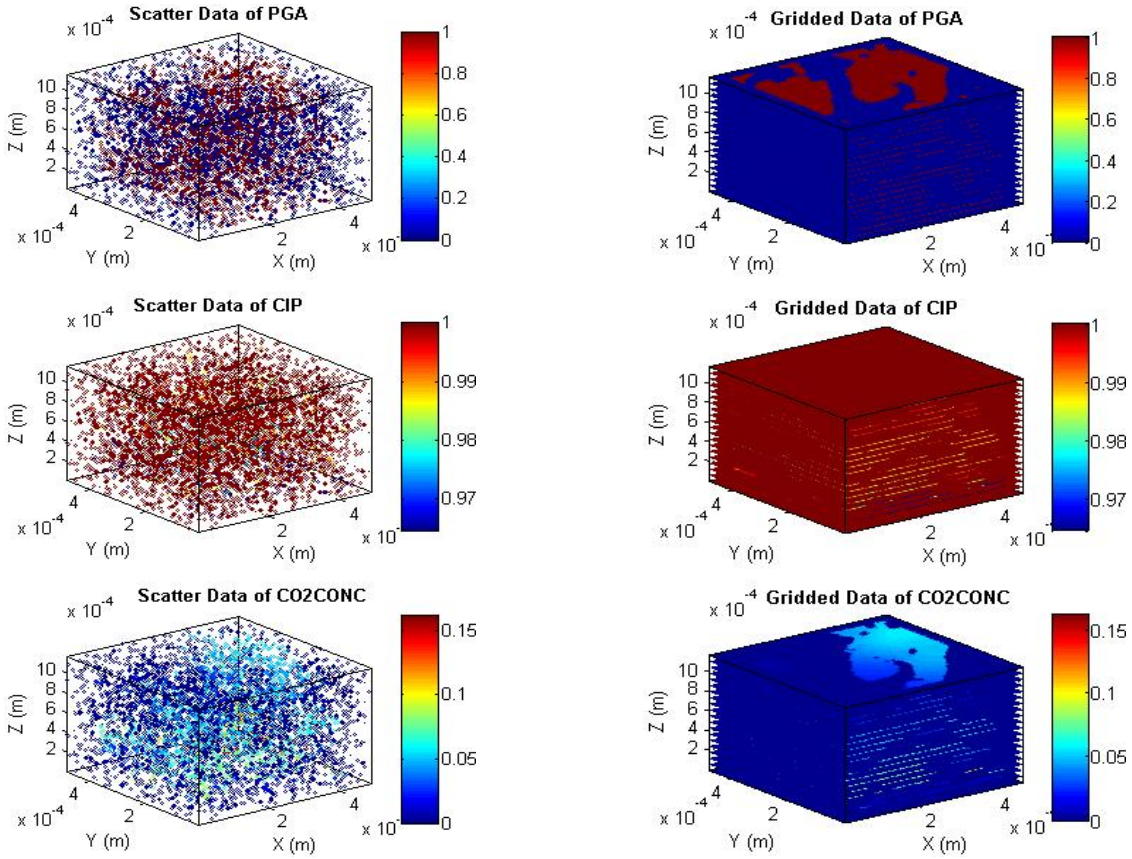

Figure 4: Pore geometry alteration - PGA (top row), change in porosity - CIP (middle row) and concentration of CO2 - CO2CONC (bottom row) in 3-D space: (a) scattered data points; (b) interpolated gridded dataset

Rock-fluid interactions cause the above attributes to change with time; therefore, the 3-D spatial datasets are interpolated at different snapshots of time from t = 0 sec to t = 20 sec. Now, to facilitate the analysis of the 3-D spatial data at various times, we retrieve three XY planes from the 3-D spatial data corresponding to each time. The slices are selected such that they exhibit the maximum spatial variation in each attribute. For each 2-D slice, we consider the variation over all time periods to obtain a 3-D spatiotemporal dataset, where the 3rd dimension now represents time. Figure 5 shows the spatiotemporal data for the three different quantities (PGA, CIP, and CO2CONC, respectively) corresponding to three different XY reference planes (Z=2, 3, and 4, respectively).

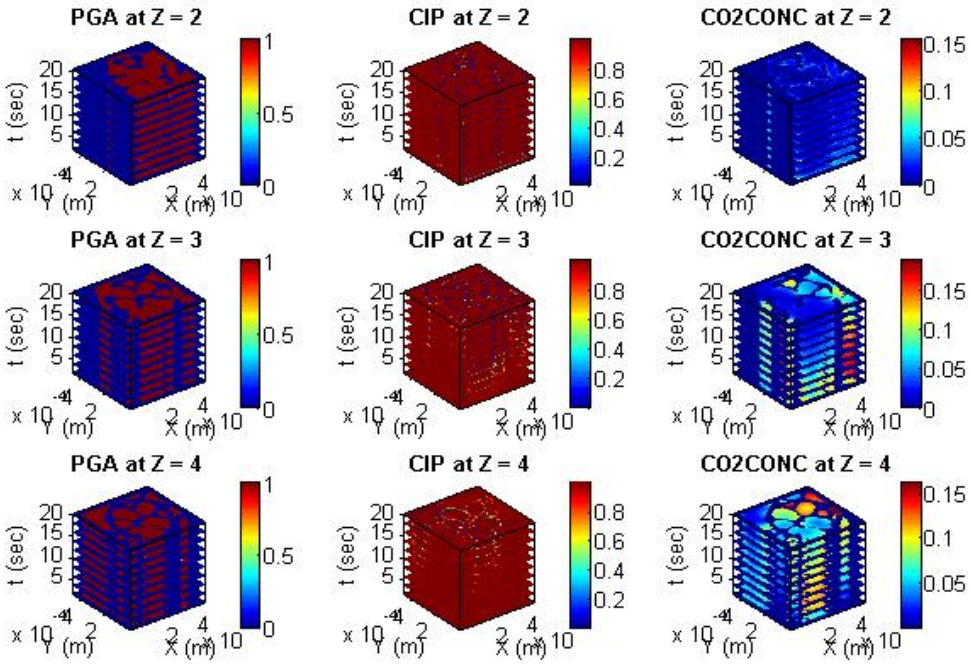

Figure 5: Gridded spatiotemporal variation of pore geometry alteration (PGA), change in porosity (CIP) and volume-based dimensionless CO_2 concentration (CO2CONC).

Ovaysi and Piri, (2014) assume a faster kinetics and they ascribe this as the reason for a significant change in both porosity and permeability in addition to the smaller sample size assumed to be completely composed of calcium carbonate. The calcium carbonate of the sample can both precipitate and dissolve, however, the highly acidic environment inside the rock results in dissolution to be the dominant process.

2.3 Estimation of REV

Here, we compare the REV scale obtained using both the spatial integration of the variogram as well as the direct averaging of fine-scale numerical values. While there is some difference among the two results because of the error in performing numerical integration and also in approximating empirical variograms using standard models, the overall profiles are quite similar. Here we establish that the direct averaging as well as the integration of variogram gives similar REV estimate. Therefore, for the remainder of this paper, only results obtained by integrating the variogram are presented, except where accurate experimental variogram cannot be attained.

2.3.1 REV Estimated from Numerical Integration of Variogram

Empirical variograms along various directions using the 3-D spatial gridded data of pressure from Figure 3 (b) are computed using the *gam* program of GSLIB library

(Deutsch and Journel, 1997). The empirical variograms along various azimuth (Θ) and dip (Φ) angles are shown in Figure 6, and a 2-D variogram slice through the 3-D modeled variogram is shown in Figure 7. It is apparent from Figure 5 that empirical variograms of the pressure attribute in the case of a conservative/nonreactive flow are nonstationary, and, therefore, empirical variograms are fitted using a nested structure of *spherical* and *power* models.

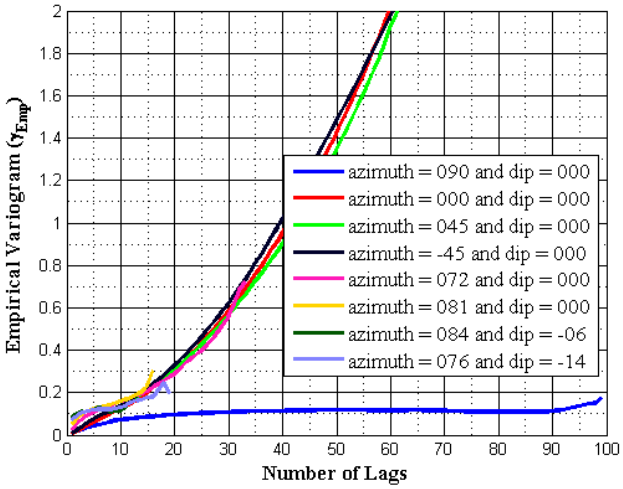

Figure 6: Empirical variograms for 3D spatial data for pressure along various azimuth (Θ) and dip (Φ) angles

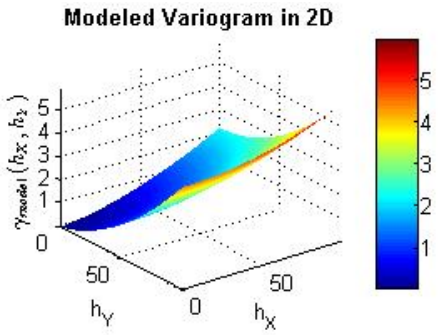

Figure 7: A projection through the 3-D variogram model computed using the spatiotemporal data for pressure

Figure 8 shows the variance of the mean computed by evaluating the convolution integral of the spatiotemporal variogram function for pressure data and plotted purely as a function of spatial lags.

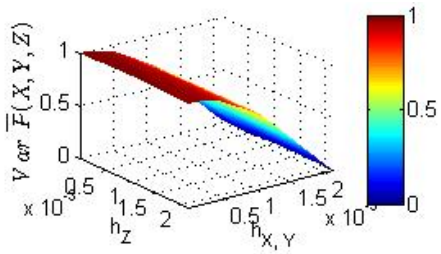

Figure 8: Variance of mean pressure computed by evaluating the spatiotemporal integral of the model covariance

The variance of the mean pressure along the diagonal of the surface plot is shown in Figure 9. This plot depicts a diagnostic signature of a negative unit slope at scales larger than and equal to REV scale. The scale at which the slope along this diagnostic plot reaches -1 provides us the volumetric REV scale, and, for this case, it corresponds to a volume of ~10^{-10} m^3 or 0.1 mm^3 (= $h_X \times h_Y \times h_Z$).

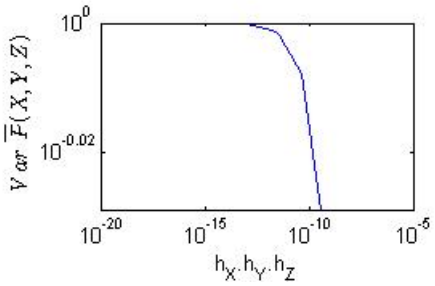

Figure 9: Variance of the mean along the diagonal of the surface plot shown in Figure 10. REV scale is achieved for a volume of ~10^{-10} m^3

2.3.2 REV Estimated Based on Averaging

2.3.2.1 Linear Averaging

For comparison purposes, REV is also obtained by directly computing the variance of the mean pressure data (without computing the covariance or variogram). For this end, we first estimate the upscaled pressure using linear (arithmetic) averaging for various spatial lags; for example, Figure 11 shows the upscaled 3-D pressure for two different grid sizes:

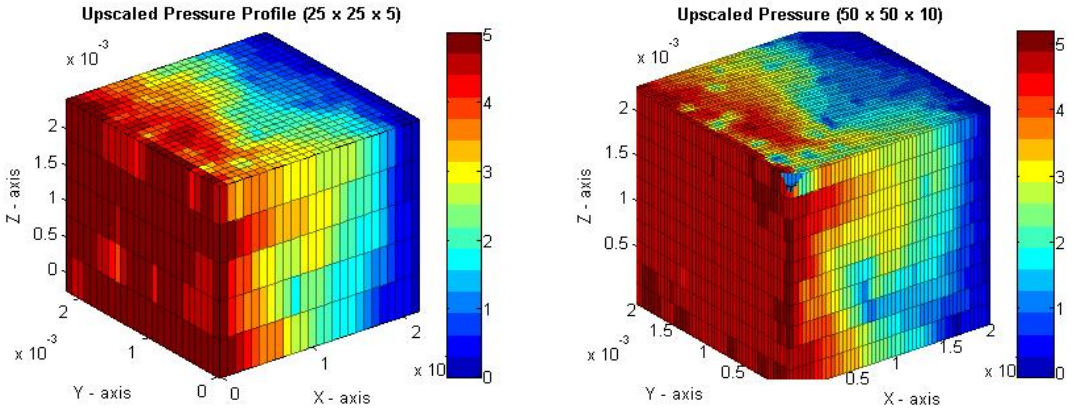

(a) (b)

Figure 11: Upscaled pressure (in Pa) based on linear averaging for number of grid blocks as a) 25 X 25 X 5, b) 50 X 50 X 10. The dimensions along X, Y and Z axes are in meter.

The variance of mean computed using linear averaging of pressure data can be presented in a surface plot against the spatial lags as shown in Figure 12, similar to that in Figure 8. The variance along the diagonal of the surface plot is shown in Figure 13.

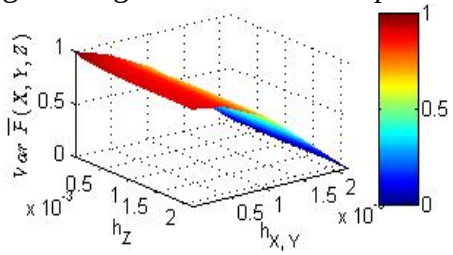

Figure 12: Variance of mean pressure computed directly using values available at the pore scale

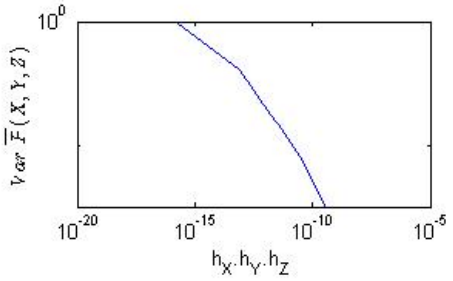

Figure 13: Variance of mean along the diagonal of the surface plot shown in Figure 12. REV scale is achieved for a volume of ~10^{-10} m^3

The minor discrepancies in the two estimated REV values (Figure 9 and Figure 13) can be attributed to the inaccuracies in numerical integration and also in

approximating empirical variograms using standard models. The scaling relationships presented in both figures indicate that the stable REV scale for this process occurs for a volume of ~10^{-10} m^3 or 0.1 mm^3 (= $h_X \times h_Y \times h_Z$).

2.3.2.2 Nonlinear Averaging

In order to examine the effect of nonlinear averaging on the REV estimation, the procedure in 3.3.2.1 is repeated using a nonlinear averaging scheme. The upscaled pressure is computed using the averaging formulation depicted in Eqn. (3) where the value of averaging exponent for nonlinear averaging is assumed as 0.5:

$$\bar{P} = \left[\frac{1}{V_b} \int_{V_b} (P)^{\omega} \, dV \right]^{1/\omega} = \left[\frac{1}{V_b} \sum_Z \sum_Y \sum_X \{P(X,Y,Z)\}^{\omega} \right]^{1/\omega} \qquad (3)$$

where,

$P(X,Y,Z)$ = Fine scale gridded pressure data

$\bar{P}$ = Upscaled pressure

V_b = Coarse block bulk volume

ω = Averaging exponent (assumed 0.5 for nonlinear averaging)

The upscaled pressure using nonlinear averaging is obtained for various spatial lags; for example, Figure 14 compares the upscaled 3-D pressure for two different grid sizes. The upscaled pressure profiles computed using nonlinear averaging are similar those computed using linear averaging in Figure 11. The similarity can be observed even with a fine grid with 50 x 50 x 10 cells.

The spatial variance of mean computed using nonlinear averaging is shown in Figure 15 in the form of a surface plot, similar to that in Figure 12. The variance along the diagonal of the surface plot of Figure 15 is shown in Figure 16.

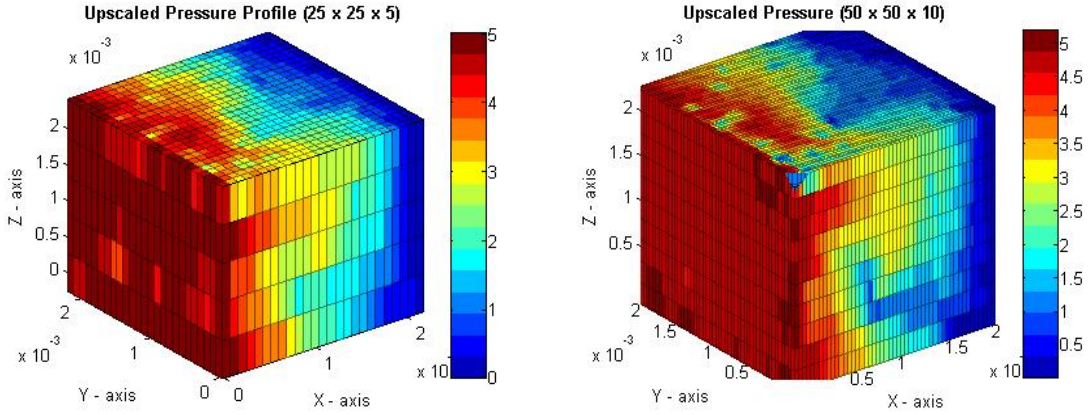

(a) (b)

Figure 14: Upscaled pressure based on nonlinear averaging for number of grid blocks as a) 25 × 25 × 5, b) 50 × 50 × 10

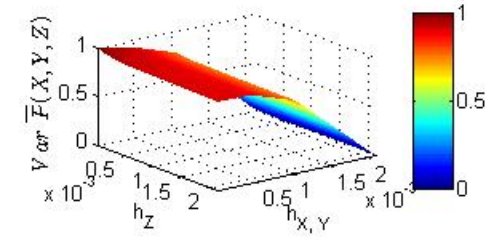

Figure 15: Variance of mean pressure computed directly using the pressure values available at the pore-scale.

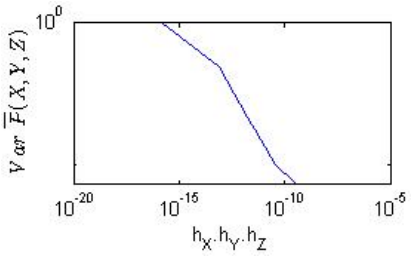

Figure 16: Variance of mean along the diagonal of the surface plot shown in Figure 15. REV scale is achieved for a volume of ~10^{-10} m^3

We compare the REV scale obtained using linear averaging and nonlinear averaging of pressure values. While there is a very slight difference in the two upscaled results because of the averaging exponent, the overall profiles and REV scales are quite similar. The stable REV scale obtained from both linear averaging and nonlinear averaging occurs for a volume of ~10^{-10} m^3 or 0.1 mm^3 (= $h_X \times h_Y \times h_Z$).

Since we have established that the direct averaging (linear or nonlinear) as well as the integration of variogram (or covariance) yield similar results, therefore, for the remaining sections only the results obtained by variogram integration are included, except where accurate variogram cannot be inferred.

2.4 Application of Spatiotemporal REV

For the purpose of illustrating the application of this method on tangible parameters, we scale-up reaction rate constant for simple first-order reaction kinetics. Reaction constant plays a significant role in reactive transport simulations; however, in most cases, value estimated at laboratory scale is directly used in field-scale simulations without accounting for the effect of change in volume support. To minimize the uncertainty (variance) in its magnitude due to spatial and temporal subscale processes, we estimate a spatiotemporal REV scale for reaction rate constant. The scaled-up reaction constant is estimated by averaging the fine scale values over the volume of spatiotemporal REV scale. This scaled-up value of reaction constant can serve as an effective quantity in reactive transport simulations.

For natural systems, reaction rate term can be highly empirical and a function of various controlling factors such as concentrations, temperature, pressure and pH (Arvidson and Luttge, 2010; Lasaga, 1998; Liu and Maroto-Valer, 2011; Morse et al., 2007). For example, for typical CO_2 mineral trapping reactions, the reaction rate could be a function of reactive surface area, activation energy, temperature and pH (Arvidson and Luttge, 2010; Lasaga, 1998; Liu and Maroto-Valer, 2011; Morse et al., 2007). The proposed scheme can be readily extended to model higher-order reaction kinetics.

2.4.1 Reaction Rate Constant at Fine-Scale

The reaction rate for a simple first order reaction is given by the following expression (Lake et al., 2002):

$$r = \alpha[c] \tag{4}$$

The first-order rate law, as shown in Eqn. (4), can describe the change in concentration with time (Lake et al., 2002):

$$-\frac{dc}{dt} = \alpha c$$

$$\Rightarrow -\int_{c=c_{ic}}^{c=c} \frac{dc}{c} = \alpha \int_{t=0}^{t=t} dt \Rightarrow -[\ln(c) - \ln(c_{ic})] = \alpha[t-0] \Rightarrow -\ln\left[\frac{c}{c_{ic}}\right] = \alpha t$$

$$\therefore \Rightarrow \alpha = -\frac{\ln\left[\frac{c}{c_{ic}}\right]}{t} \tag{5}$$

where,

r = reaction rate

α = reaction rate constant

c = volume-based dimensionless concentration of CO_2 at time t

c_{ic} = volume-based dimensionless initial concentration of CO_2 at time t = 0

Using the expression for α shown in Eqn. (5) and the pore-scale CO_2 concentration data, a scale-up procedure for α is formulated.

2.4.2 Procedure to Obtain Spatiotemporal REV of Reaction Rate Constant

The statistical scale-up method described above is extended to scale-up reaction rate constant across spatial and temporal scales. An upscaled or effective reaction rate constant is computed using the following two algorithms:

i. Algorithm-1: Compute linearly-averaged concentration data (CO2CONC) for a given coarse block size of the spatial and temporal grids. Denoting the resultant upscaled concentration value corresponding to a particular spatiotemporal REV scale as $\overline{c}(s;t)$ and replacing c in Eqn. (5) with $\overline{c}(s;t)$, the upscaled reaction rate constant $\overline{\alpha}(s;t)$

can be computed following Eqn. (6). The scaling relationship of $\bar{\alpha}(s;t)$ is estimated by repeating this procedure for different coarse block size of the spatial and temporal grids.

$$\bar{\alpha}(s;t) = -\frac{\ln\left[\dfrac{\bar{c}(s;t)}{c_{ic}}\right]}{t} \tag{6}$$

ii. Algorithm-2: Compute the fine scale reaction rate constant, $\alpha(s;t)$, by substituting the fine scale concentration data, $c(s;t)$, in Eqn. (5). $\bar{\alpha}(s;t)$ is computed via linear averaging for a particular coarse block size of the spatial and temporal grids.

Algorithm-2 is not recommended because it assumes that α averages linearly in space and time, but there is no physical basis for this assumption.

3 RESULTS AND DISCUSSION

The REV scales for three reactive attributes (- PGA, CIP, and CO2CONC) are computed using the 3-D spatiotemporal data. Scale-up of reaction rate constant is performed using Algorithm-1 described earlier.

3.1 REV Scales With Reactive Dynamics

We compute empirical variograms along several spatial and temporal lags using the 3-D spatiotemporal data of Figure 5. The empirical variograms of PGA, CIP and CO2CONC along a few randomly-selected directions are shown in Figure 17. Second-order stationarity is observed in Figure 17 for all three attributes, and their corresponding empirical variograms are fitted using the *spherical* model, as shown in Figure 18.

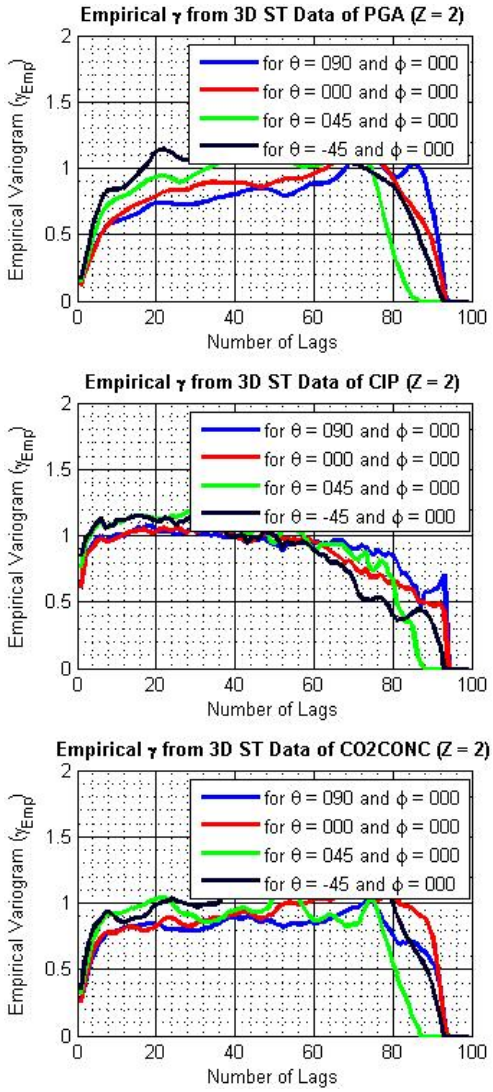

Figure 17: Empirical variograms of PGA (top), CIP (middle) and CO2CONC (bottom) computed using the spatiotemporal data for the reactive process along various azimuth (Θ) and dip (Φ) angles

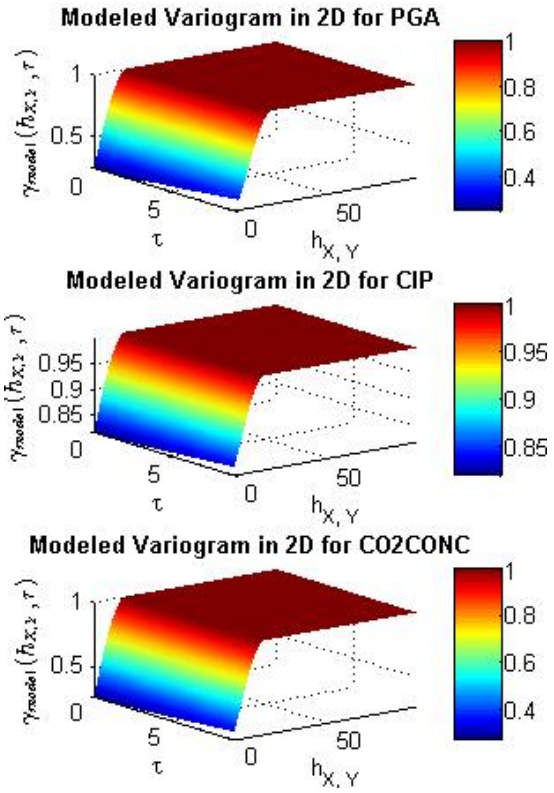

Figure 18: Spatiotemporal variogram models for PGA (top), CIP (middle) and CO2CONC (bottom)

The spatiotemporal variance of the mean profiles computed by numerical integration of the spatiotemporal variogram over all spatial and temporal lags are shown in Figure 19 through Figure 21 for the three attributes, PGA, CIP, and CO2CONC, respectively. Results for Figure 20 are divided into two figures - Figure 20 (a) obtained by the integration of the spatiotemporal variogram function over all spatial and temporal lags, and Figure 20 (b) obtained by linearly averaging the CIP data available at the pore-scale. This exception of showing variance of mean by two methods in Figure 20 is made because the spatiotemporal variogram could not be modeled accurately for the CIP data.

Each of the three figures from Figure 19 through Figure 21 also shows a section along the diagonal of the surface plot. These surface plots show that the curvature (of the variance of mean profile) at higher temporal lags differs significantly from the curvature at small temporal lags, indicating that the REV scale (scale at which slope of curvature reaches negative one) changes with time. It is possible that this temporal change in REV is due to the alteration in pore structure by the reactive processes, such as those associated with CO_2 storage in geological formations. This result highlights the significance of including both the spatial and temporal scales in estimating an REV scale in presence of pore-altering processes.

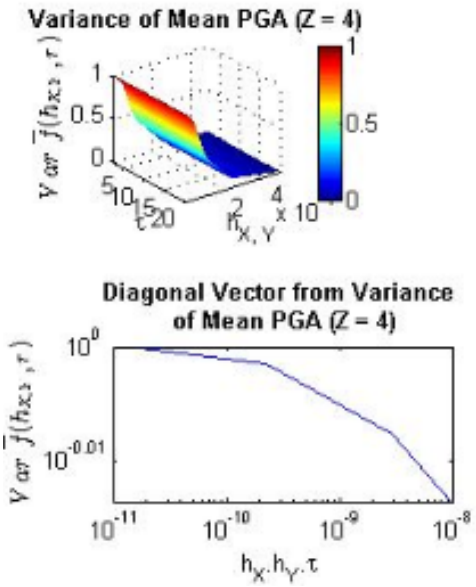

Figure 19: Spatiotemporal variance of mean PGA by numerical integration of the spatiotemporal variogram model over various spatial and temporal lags.

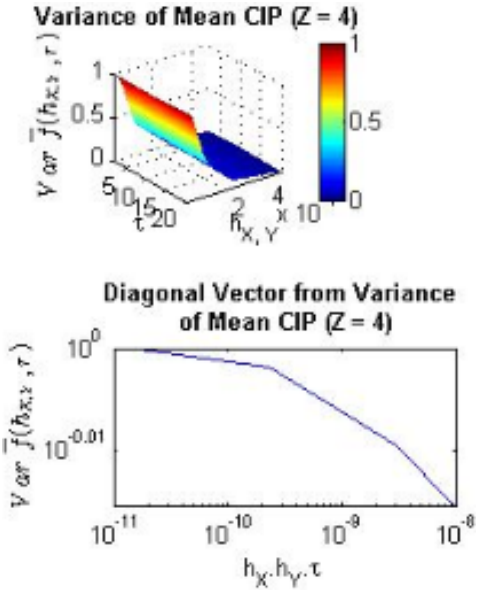

Figure 20 (a): Spatiotemporal variance of mean CIP by numerical integration of the spatiotemporal variogram model over various spatial and temporal lags.

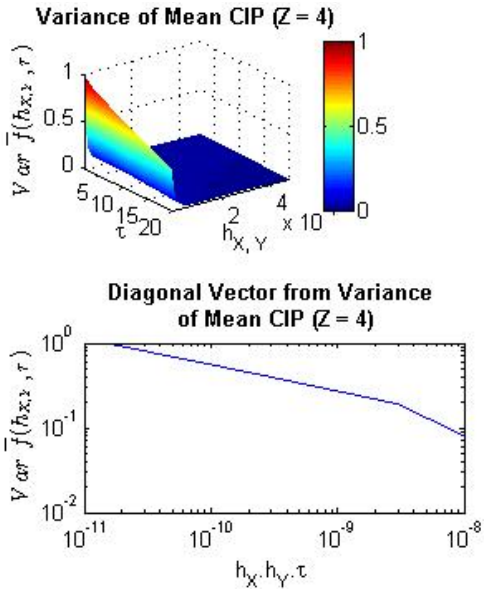

Figure 18 (b): Spatiotemporal variance of mean CIP by linear averaging of the pore-scale data.

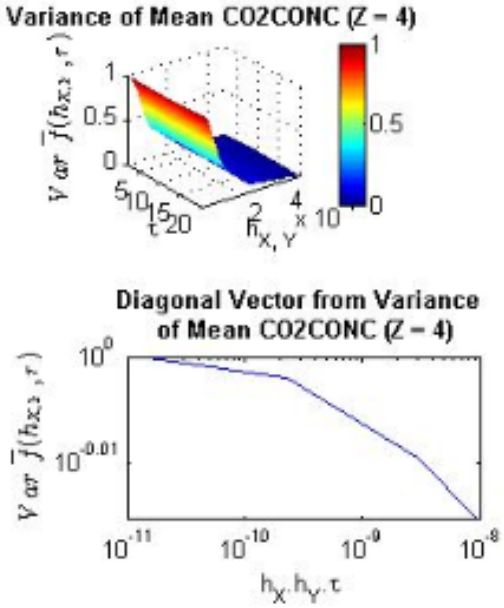

Figure 21: Spatiotemporal variance of mean CO2CONC by numerical integration of the spatiotemporal variogram model over various spatial and temporal lags.

The REV profiles indicate that the stable REV scale for PGA (Figure 19) and CO2CONC (Figure 21) corresponds to a spatiotemporal volume of ~3 X 10^{-9} m^2-sec or 3

X 10^{-3} mm^2-sec (= $h_X \times h_Y \times \tau$), whereas, the stable REV scale for the attribute CIP, as shown in Figure 20 (b), corresponds to a spatiotemporal volume of ~10^{-8} m^2-sec or 10 mm^2-sec (= $h_X \times h_Y \times \tau$). The two attributes of PGA and CO2CONC are exhibiting similar scaling behavior because CO2CONC contains information representing the presence of fluid in the pore space and, hence, effectively acts as a proxy for the pore space, whereas the actual pore space data is also represented by the attribute of PGA in this work. On the contrary, the attribute of CIP scales differently than the other two attributes because dissolution is a complex function of fluid composition, rock mineralogy and reservoir conditions. Its corresponding REV scale is so much greater than the REV scale of other two attributes (PGA and CO2CONC) because dissolution alters the pore structure and, therefore, introducing more heterogeneity into the porous medium that is translated into a larger REV scale.

3.2 Application of Spatiotemporal REV: Reaction Rate Constant

Spatiotemporal REV for reaction rate constant is obtained according to algorithm-1 in section 2.4.2. The surface plots of the variance of mean profile against the spatiotemporal lags are presented in Figure 22.

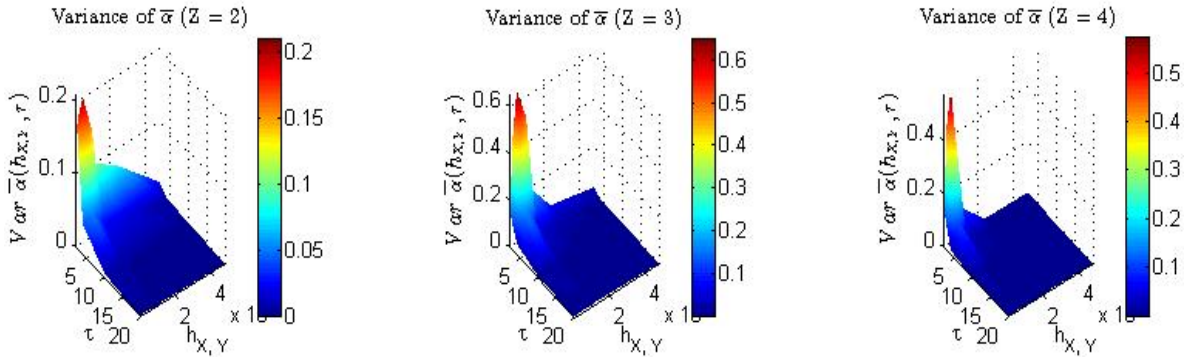

Figure 22: Variance of mean reaction rate constant computed using averaged concentrations corresponding to different spatial scales.

The spatiotemporal variance of the mean reaction rate constant along the diagonal of the surface plots is shown in Figure 23. A stable REV scale corresponding to a spatiotemporal volume of ~4x10^{-9} m^2-sec or 4x10^{-3} mm^2-sec (= $h_X \times h_Y \times \tau$) can be inferred.

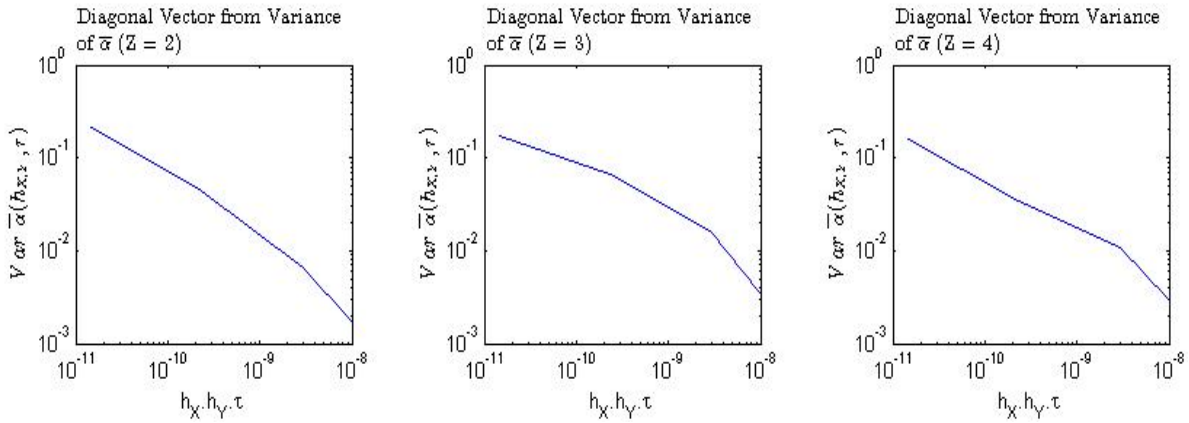

Figure 23: Variance of mean reaction rate constant computed using algorithm-1.

The REV spatiotemporal volume of ~4×10^{-9} m^2-sec for reaction rate constant (shown in Figure 23) and the REV spatiotemporal volume of ~3×10^{-9} m^2-sec for CO_2 concentration (shown in Figure 21) are reasonably similar. This similarity in REVs of reaction rate constant and CO_2 concentration could be due to the fact that reaction rate constant in Eqn. (5) is a function of only one dependent variable, which is concentration. If the reaction rate constant is a complex function of more than one dependent variable such as reactive surface area, temperature, pressure and pH, it is possible that the REV scale of reaction rate constant may have a complex dependence on the REV scale of each dependent variable, which forms the expression of reaction rate constant.

The purpose of computing REV scale of reaction rate constant is to obtain a single scaled-up value of reaction rate constant that can be used as input in reactive transport simulations. This scaled-up value of reaction rate constant will minimize the uncertainties arising due to sub-processes associated with reaction rate constant. We can minimize those uncertainties in two ways:

i. Utilizing a single scaled-up value of reaction rate constant at REV scale – considering a combined space-time REV scale of reaction constant and splitting the combined spatiotemporal scale into individual spatial and temporal scales, algorithm-1 is used to scale up the reaction rate constant.
ii. Selecting the magnitude of spatial and temporal discretizations for numerical simulations of reactive processes in a way that their product is equal to or greater than the REV scale of the reaction rate constant.

This work has demonstrated an application of the proposed method to scale up reaction rate constant from pore-scale data. Since subsurface heterogeneous features often occur at vastly different scales, in order to understand the scaling characteristics of reactive flow at the field scale, a framework that entails the modeling to be broken down into a hierarchy of scales might be adopted.

4 CONCLUSIONS

The scaling characteristics of the conservative and reactive processes were investigated using pore-scale CO_2-rock interaction data. This study presented a method to obtain the REV of a rock property by accounting for spatial and temporal variations in that property due to reactive kinetics. We illustrate the application of the proposed spatiotemporal REV on a tangible parameter like reaction rate constant that is useful in reactive flow simulations. The implications of results presented in this study suggest that a robust assessment of REV for rocks with reactive dynamics should involve coupling of temporal scale with spatial scale.

The first-order kinetic equation is only valid when the surface area is constant for the rocks. However, for natural subsurface rocks the surface area is likely to be a function of scale, so the reaction kinetic equation would be of the form $r = \alpha S(1 - c)$, where S changes with scale. Therefore, the future research should focus on how this complexity in reaction kinetics would affect the scale dependence of reaction rate constant.

5 ACKNOWLEDGMENT

This research is based upon work supported by the Center for Frontiers of Subsurface Energy Security (CFSES), UT Austin, funded by Basic Energy Sciences at the U.S. Department of Energy. The authors would like to thank Saeed Ovaysi, Sanjay Srinivasan, and Mary Wheeler for providing the pore-scale data for this research.

6 REFERENCES

Arsyad, A., Mitani, Y., Babadagli, T., 2013. Comparative Assessment of Potential Ground Uplift Induced by Injection of CO2 into Ainoura, and Berea Sandstone Formations. *Procedia Earth and Planetary Science*, *6*, 278–286. https://doi.org/10.1016/j.proeps.2013.01.037

Arvidson, R. S., Luttge, A., 2010. Mineral dissolution kinetics as a function of distance from equilibrium – New experimental results. *Chemical Geology*, *269*(1–2), 79–88. https://doi.org/10.1016/j.chemgeo.2009.06.009

Bear, J., 1972. *Dynamics of fluids in porous media*. American Elsevier Pub. Co.

Blumenfeld, R., Blunt, M., Bijeljic, B., et al., 2013. *Imperial College consortium on pore-scale modeling* (Yearly Progress Report). London, UK: Imperial College.

Chou, L., Garrels, R. M., Wollast, R., 1989. Comparative study of the kinetics and mechanisms of dissolution of carbonate minerals. *Chemical Geology*, *78*(3–4), 269–282. https://doi.org/10.1016/0009-2541(89)90063-6

Davis, M. C., Wesolowski, D. J., Rosenqvist, J., et al., 2011. Solubility and near-equilibrium dissolution rates of quartz in dilute NaCl solutions at 398–473 K under alkaline conditions. *Geochimica et Cosmochimica Acta*, *75*(2), 401–415. https://doi.org/10.1016/j.gca.2010.10.023

Deutsch, C. V., Journel, A. G., 1997. *GSLIB: Geostatistical Software Library and User's Guide* (2nd ed.). Oxford University Press, USA.

Dong, H., 2007. *Micro CT Imaging and Pore Network Extraction* (PhD Dissertation). Imperial College London, London, UK.

Ellis, B. R., Crandell, L. E., Peters, C. A., 2010. Limitations for brine acidification due to SO2 co-injection in geologic carbon sequestration. *International Journal of Greenhouse Gas Control*, *4*(3), 575–582. https://doi.org/10.1016/j.ijggc.2009.11.006

Gunter, W. D., Wiwehar, B., Perkins, E. H., 1997. Aquifer disposal of CO2-rich greenhouse gases: Extension of the time scale of experiment for CO2-sequestering reactions by geochemical modelling. *Mineralogy and Petrology*, *59*(1–2), 121–140. https://doi.org/10.1007/BF01163065

Izgec, O., Demiral, B., Bertin, H., et al., 2005. CO2 Injection in Carbonates. In *Proceedings of SPE Western Regional Meeting*. https://doi.org/10.2118/93773-MS

Izgec, O., Demiral, B., Bertin, H., et al., 2007. CO2 Injection into Saline Carbonate Aquifer Formations II: Comparison of Numerical Simulations to Experiments. *Transport in Porous Media*, *73*(1), 57–74. https://doi.org/10.1007/s11242-007-9160-1

Johnson, J. W., Nitao, J. J., Knauss, K. G., 2004. Reactive transport modelling of CO2 storage in saline aquifers to elucidate fundamental processes, trapping mechanisms and sequestration partitioning. *Geological Society, London, Special Publications*, *233*(1), 107–128. https://doi.org/10.1144/GSL.SP.2004.233.01.08

Kim, E., 2012. *Investigation of CO2 Seeps at the Crystal Geyser Site Using Numerical Modeling with Geochemistry* (Thesis). The University of Texas at Austin, Austin, Texas.

Knauss, K. G., Wolery, T. J., 1988. The dissolution kinetics of quartz as a function of pH and time at 70°C. *Geochimica et Cosmochimica Acta*, *52*(1), 43–53. https://doi.org/10.1016/0016-7037(88)90055-5

Lake, L. W., Bryant, S. L., Araque-Martinez, A. N., 2002. *Geochemistry and Fluid Flow*. Elsevier.

Lake, L. W., Srinivasan, S., 2004. Statistical scale-up of reservoir properties: concepts and applications. *Journal of Petroleum Science and Engineering*, *44*(1–2), 27–39. https://doi.org/10.1016/j.petrol.2004.02.003

Lasaga, A. C., 1998. *Kinetic Theory in the Earth Sciences*. Princeton University Press.

Le Borgne, T., Gouze, P., 2008. Non-Fickian dispersion in porous media: 2. Model validation from measurements at different scales. *Water Resources Research*, *44*(6), W06427. https://doi.org/10.1029/2007WR006279

Leung, J., Srinivasan, S., 2011. Analysis of Uncertainty Introduced by Scaleup of Reservoir Attributes and Flow Response in Heterogeneous Reservoirs. *SPE Journal*. https://doi.org/10.2118/145678-PA

Li, L., Steefel, C. I., Yang, L., 2008. Scale dependence of mineral dissolution rates within single pores and fractures. *Geochimica et Cosmochimica Acta*, *72*(2), 360–377. https://doi.org/16/j.gca.2007.10.027

Lichtner, P. C., Steefel, C. I., Oelkers, E. H., 1996. *Reactive transport in porous media*. Washington, DC: Mineralogical Society of America.

Liu, Q., Maroto-Valer, M. M., 2011. Parameters affecting mineral trapping of CO2 sequestration in brines. *Greenhouse Gases: Science and Technology*, *1*(3), 211–222. https://doi.org/10.1002/ghg.29

Miri, R., van Noort, R., Aagaard, P., et al., 2015. New insights on the physics of salt precipitation during injection of CO2 into saline aquifers. *International Journal of Greenhouse Gas Control*, *43*, 10–21. https://doi.org/10.1016/j.ijggc.2015.10.004

Morse, J. W., Arvidson, R. S., Lüttge, A., 2007. Calcium Carbonate Formation and Dissolution. *Chemical Reviews*, *107*(2), 342–381. https://doi.org/10.1021/cr050358j

Øren, P.-E., Bakke, S., 2003. Reconstruction of Berea sandstone and pore-scale modelling of wettability effects. *Journal of Petroleum Science and Engineering*, *39*(3–4), 177–199. https://doi.org/10.1016/S0920-4105(03)00062-7

Ovaysi, S., Piri, M., 2010. Direct pore-level modeling of incompressible fluid flow in porous media. *Journal of Computational Physics*, *229*(19), 7456–7476. https://doi.org/10.1016/j.jcp.2010.06.028

Ovaysi, S., Piri, M., 2011. Pore-scale modeling of dispersion in disordered porous media. *Journal of Contaminant Hydrology*, *124*(1–4), 68–81. https://doi.org/10.1016/j.jconhyd.2011.02.004

Ovaysi, S., Piri, M., 2013. Pore-scale dissolution of CO2 + SO2 in deep saline aquifers. *International Journal of Greenhouse Gas Control*, *15*, 119–133. https://doi.org/10.1016/j.ijggc.2013.02.009

Ovaysi, S., Piri, M., 2014. Pore-space alteration induced by brine acidification in subsurface geologic formations. *Water Resources Research*, *50*(1), 440–452. https://doi.org/10.1002/2013WR014289

Pham, T., Aagaard, P., Hellevang, H., 2012. On the potential for CO2 mineral storage in continental flood basalts – PHREEQC batch- and 1D diffusion–reaction simulations. *Geochemical Transactions*, *13*(1), 5. https://doi.org/10.1186/1467-4866-13-5

Pham, V. T. H., Lu, P., Aagaard, P., Zhu, C., Hellevang, H., 2011. On the potential of CO2–water–rock interactions for CO2 storage using a modified kinetic model. *International Journal of Greenhouse Gas Control*, *5*(4), 1002–1015. https://doi.org/10.1016/j.ijggc.2010.12.002

Rathnaweera, T. D., Ranjith, P. G., Perera, M. S. A., 2016. Experimental investigation of geochemical and mineralogical effects of CO2 sequestration on flow characteristics of reservoir rock in deep saline aquifers. *Scientific Reports*, *6*, 19362. https://doi.org/10.1038/srep19362

Rochelle, C. A., Czernichowski-Lauriol, I., Milodowski, A. E., 2004. The impact of chemical reactions on CO2 storage in geological formations: a brief review. *Geological Society, London, Special Publications*, *233*(1), 87–106. https://doi.org/10.1144/GSL.SP.2004.233.01.07

Shipton, Z. K., Evans, J. P., Kirschner, D., et al., 2004. Analysis of CO2 Leakage Through “low-Permeability” Faults from Natural Reservoirs in the Colorado Plateau, East-Central Utah. *Geological Society, London, Special Publications*, *233*(1), 43–58. https://doi.org/10.1144/GSL.SP.2004.233.01.05

Singh, H., 2014. *Scale-up of reactive processes in heterogeneous media* (Dissertation). The University of Texas at Austin.

Singh, H., Srinivasan, S., 2014a. Scale up of Reactive Processes in Heterogeneous Media - Numerical Experiments and Semi-analytical Modeling. Presented at the SPE Improved Oil Recovery Symposium, Tulsa, Oklahoma, USA: Society of Petroleum Engineers. https://doi.org/10.2118/169133-MS

Singh, H., Srinivasan, S., 2014b. Some perspectives on Scale-up of Flow and Transport in Heterogeneous Media. *Bulletin of Canadian Petroleum Geology*.

Sund, N. L., Bolster, D., Dawson, C., 2015. Upscaling transport of a reacting solute through a peridocially converging–diverging channel at pre-asymptotic times. *Journal of Contaminant Hydrology*, *182*, 1–15. https://doi.org/10.1016/j.jconhyd.2015.08.003

TriScatteredInterp., R2013b. MathWorks. Retrieved from http://www.mathworks.com/help/matlab/ref/triscatteredinterp.html

Vishal, V., Leung, J. Y., 2015. Modeling impacts of subscale heterogeneities on dispersive solute transport in subsurface systems. *Journal of Contaminant Hydrology*, *182*, 63–77. https://doi.org/10.1016/j.jconhyd.2015.08.006